

Turbulence Measurements from Compliant Moorings - Part II: Motion

Correction

Levi Kilcher*, Jim Thomson, Samuel Harding, and Sven Nylund

**Corresponding author address:* National Renewable Energy Laboratory, Golden, Colorado

E-mail: Levi.Kilcher@nrel.gov

ABSTRACT

6 Acoustic Doppler velocimeters (ADV) are a valuable tool for making high-
7 precision measurements of turbulence, and moorings are a convenient and
8 ubiquitous platform for making many kinds of measurements in the ocean.
9 However—because of concerns that mooring motion can contaminate tur-
10 bulence measurements and acoustic Doppler profilers are relatively easy to
11 deploy—ADVs are not frequently deployed from moorings. This work de-
12 tails a method for measuring turbulence using moored ADVs that corrects
13 for mooring motion using measurements from inertial motion sensors. Three
14 distinct mooring platforms were deployed in a tidal channel with inertial-
15 motion-sensor-equipped ADVs. In each case, the motion correction based on
16 the inertial measurements dramatically reduced contamination from mooring
17 motion. The spectra from these measurements have a shape that is consistent
18 with other measurements in tidal channels, and have a $f^{-5/3}$ slope at high
19 frequencies—consistent with Kolmogorov’s theory of isotropic turbulence.
20 Motion correction also improves estimates of cross-spectra and Reynold’s
21 stresses. Comparison of turbulence dissipation with flow speed and turbu-
22 lence production indicates a bottom boundary layer production-dissipation
23 balance during ebb and flood that is consistent with the strong tidal forcing
24 at the site. These results indicate that inertial-motion-sensor-equipped ADVs
25 are a valuable new tool for measuring turbulence from moorings.

26 1. Introduction

27 Acoustic Doppler velocimeters (ADV) have been used to make high-precision measurements of
28 water velocity for over 20 years (Kraus et al. 1994; Lohrmann et al. 1995). During that time, they
29 have been deployed around the world to measure turbulence from a range of platforms, including
30 stationary structures on ocean- and lake-bottoms, in surface waters from a pole lowered from
31 a ship's bow, and in the deep ocean from autonomous underwater vehicles (e.g., Voulgaris and
32 Trowbridge 1998; Zhang et al. 2001; Kim et al. 2000; Goodman et al. 2006; Lorke 2007; Geyer
33 et al. 2008; Cartwright et al. 2009).

34 A relatively small fraction of ADV measurements have been made from moorings (e.g., Fer
35 and Paskyabi 2014). Presumably this is because mooring motion can contaminate ADV mea-
36 surements, and acoustic Doppler profilers (ADPs) can be used to measure mid-depth turbulence
37 statistics without a mooring (e.g., Stacey et al. 1999a; Rippeth et al. 2002; Wiles et al. 2006).
38 Still, ADV measurements have distinct characteristics that can be advantageous: they are capa-
39 ble of higher sample rates, have higher signal-to-noise ratios, and have a much smaller sample
40 volume (1 centimeter, as opposed to several meters). That is, compared to an ADP, ADVs are
41 high-precision instruments capable of providing unique information. They could be more widely
42 used as a moored instrument (i.e., at an arbitrary depth) if a method for accounting for mooring
43 motion can be demonstrated to provide more accurate estimates of turbulence statistics.

44 Inertial motion unit (IMU) sensors have been used in the aerospace and aeronautical industries
45 to quantify the motion of a wide range of systems for several decades (Bevly 2004). Over the
46 last 10 years, the smartphone, drone, and 'Internet of Things' markets has driven innovation in
47 microelectrical-mechanical systems, including the IMU. As a result of this growth and innovation
48 the cost, power requirements, and size of IMUs have come down. Also known as MARG (mag-

netic, angular-rate, gravity), or AHRS (attitude heading reference system) sensors, IMUs measure three axes of the Earth’s magnetic field, angular rotation, and linear acceleration.¹ These signals are then integrated using Kalman filters to estimate the orientation and motion of the sensor (Barshan and Durrant-Whyte 1995; Marins et al. 2001; Bachmann et al. 2003).

Nortek now offers a version of their Vector ADV with a Microstrain 3DM-GX3-25 IMU sensor (Nortek 2005; MicroStrain 2012). The IMU’s signals are incorporated into the Vector data stream so that the motion and orientation signals are tightly synchronized with the ADV’s velocity measurements. This tight synchronization provides a data stream that can be utilized to quantify ADV motion in the Earth’s inertial reference frame, and remove that motion from the ADV’s velocity measurements at each time step of its sampling. This work specifies a method for performing motion correction of these ‘ADV-IMU’ measurements, and presents results of this method using data from a range of mooring configurations that positioned ADV-IMUs at mid-depths in Puget Sound.

This effort was originally motivated by a need for low-cost, high-precision turbulence measurements for the emerging tidal energy industry (McCaffrey et al. 2015; Alexander and Hamlington 2015). Experience in the wind energy industry has shown that wind turbine lifetime is reduced by atmospheric turbulence, and the same is expected to be true for tidal energy turbines. In wind, meteorological towers are often used to position sonic anemometers at the hub height of wind turbines for measuring detailed turbulence inflow statistics (Hand et al. 2003; Kelley et al. 2005; Mücke et al. 2011; Afgan et al. 2013). In the ocean, tower-mounted hub-height turbulence measurements have been made, but they are challenging to install and maintain in energetic tidal sites (Gunawan et al. 2014; Thomson et al. 2012). Therefore, the U.S. Department of Energy funded this work to

¹Within this literature, IMU is generally reserved for a MARG sensor without a magnetometer, but herein we refer to the entire group of sensors that measure motion using accelerometers and angular-rate sensors as IMUs.

71 investigate the accuracy of mooring-deployed ADV-IMUs to reduce the cost of turbulence mea-
72 surements at tidal energy sites (Kilcher et al. 2016). The approach proved to be successful and
73 potentially useful to the broader oceanographic community interested in moored turbulence mea-
74 surements (Lueck and Huang 1999; Doherty et al. 1999; Nash et al. 2004; Moum and Nash 2009;
75 Alford 2010; Paskyabi and Fer 2013).

76 The next section describes details of the measurements, including a summary of the hardware
77 configurations (platforms) that were used to support and position the ADV-IMUs in the water
78 column. A detailed description of the motion of these platforms is found in the companion paper to
79 this work, Harding et al. (in review), hereafter Part 1. Section 3 describes the mathematical details
80 of motion correction and Section 4 presents results from applying the method to measurements
81 from the various platforms. Section 5 is a discussion of the energetics of the tidal channel in
82 which the measurements were made and demonstrates that the measurements are consistent with
83 turbulence theory and other measurements in similar regimes. A summary and concluding remarks
84 are provided in Section 6.

85 **2. Measurements**

86 This work focuses on measuring turbulence from ADVs that are deployed from nonstationary
87 platforms and equipped with IMUs. The ADVs utilized for these measurements were equipped
88 with Microstrain 3DM-GX3-25 IMU sensors that captured all six components of the ADV mo-
89 tion (three components of angular rotation and three components of linear acceleration), as well
90 as the orientation of the ADV pressure case. The sampling of the motion sensor is tightly syn-
91 chronized with the ADV measurements. The IMU measures its motion at 1 kHz and uses internal
92 signal integration (Kalman filtering) to output the motion signals at the same sample rate as the
93 ADV's velocity measurements. This reduces aliasing of the IMU's motion measurements above

94 the ADV's sample rate (MicroStrain 2010). Cable-head ADVs were used throughout this work to
95 allow for flexibility in the positioning of the ADV head relative to its pressure case.

96 All measurements used in this work were made in Admiralty Inlet, Washington, approximately
97 500 m west southwest of Admiralty Head in 60-m of water near 48° 9.18' N, 122° 41.22' W
98 (Figure 1). The site is approximately 6 km east of Port Townsend, and 1 km north of the Port
99 Townsend to Coupeville ferry route. Admiralty inlet is the largest waterway connecting Puget
100 Sound to the Strait of Juan de Fuca, and it possesses a large semidiurnal tidal flow (Thomson
101 et al. 2012; Polagye and Thomson 2013). This work utilizes data from three distinct deployment
102 platforms: the tidal turbulence mooring, a StableMoor buoy, and a simple sounding weight. All
103 data used in this analysis is available from the MHK data repository (<http://mhkdr.openei.org>;
104 submission ids: 49, 50 and 51). Additional details, photos, and schematic diagrams of all three
105 mooring systems can be found in Part 1.

106 *a. Tidal Turbulence Mooring*

107 The tidal turbulence mooring (TTM) is a simple mooring system with a strongback fin sus-
108 pended between a steel clump-weight anchor weighing 1,200 kg when dry and a 0.93-m-diameter
109 spherical steel buoy with a buoyancy of 320 kg. The ADV pressure cases were clamped to one
110 side of the strongback fin and the ADV sensor head was positioned 10 cm in front of the fin's
111 leading edge (Figure 2). The leading edge of the fin is fastened inline with the mooring line. This
112 configuration was designed to work like a weather vane, such that the drag on the fin held the ADV
113 head upstream of the mooring components. This work utilizes data from two TTM deployments.

114 1) JUNE 2012 TTM DEPLOYMENT

115 The first TTM deployment was in June 2012 from 17:30 on the 12th until 14:30 on the 14th
116 (local; i.e., Pacific Daylight Time). Two Nortek ADVs were clamped to either side of the fin so that
117 the axis of their cylindrical pressure cases were parallel with the leading edge of the strongback.
118 The ADV heads were spaced 0.5 m apart vertically along the fin. Only one of these ADVs was
119 equipped with an integrated IMU. This TTM also had an upward-looking acoustic Doppler profiler
120 mounted on the mooring anchor.

121 Periods of time during which this mooring interfered with a beam of the Doppler profiler were
122 identified by inspecting the profiler's acoustic amplitude signal. Periods during which one beam
123 of the profiler had $> 5\%$ higher acoustic amplitude than the other beams were flagged as "contam-
124 inated" and excluded from averaging. Five-minute averages in which more than 50% of the data
125 were contaminated in this way were masked as invalid.

126 2) JUNE 2014 TTM DEPLOYMENT

127 The second TTM deployment was in 2014 from 06:00 on June 17 to 05:00 on June 19 (local
128 time). Two Nortek ADV-IMUs were mounted on this TTM, with their heads spaced 0.5 m apart
129 along the fin. In this case, the pressure cases and ADV heads were inclined at an angle of 18° to
130 the leading edge of the fin to account for mooring blowdown during strong currents (Figure 3).
131 This change was made to reduce vibrational motion observed during the June 2012 deployment
132 that was believed to be associated with the orientation of the pressure cases.

133 *b. The StableMoor platform*

134 The second deployment platform was a cylindrical, StableMoor, syntactic foam buoy (manufac-
135 turer: Deep Water Buoyancy) that was anchored to a clump weight that weighed 2,700 lbs (Figure

136 4). The buoy is 3.5 m long and 0.45 m in diameter with a tail ring that is 0.76 m in diameter. The
137 StableMoor buoy weighs 295 kg in air, and has a buoyancy of 185 kg in water.

138 The StableMoor buoy was deployed with an ADV-IMU mounted at its nose from 11:21 on May
139 12 to 11:53 on May 13, 2015 (local time). The sample volume of the ADV is 10 cm forward of
140 the nose and 20 cm above the center line of the StableMoor buoy (Figure 4). Based on Wyngaard
141 et al.'s (1985) investigation of a similarly shaped slender body, the velocity measurements should
142 have flow-distortion effects of less than 10%. This configuration was designed to be the most
143 stable platform for measuring turbulence from a moving platform. The StableMoor buoy was
144 equipped with a 1,200-kHz RDI workhorse sentinel acoustic Doppler profiler that was oriented
145 downward-looking to measure water velocity below the platform in twelve 1-m bins and measure
146 buoy motion ("bottom tracking"), all at a 1-Hz sample rate.

147 The buoy was ballasted to pitch upward a few degrees in zero-flow to avoid "flying downward."
148 In the presence of an oncoming current, the tail fins help to orient it into the flow. The anchor for
149 this buoy is similar to that of the TTM, including an acoustic release so the mooring and anchor
150 can be recovered separately.

151 The StableMoor platform has two primary advantages compared to the TTM. First, it is signif-
152 icantly more massive and hydrodynamically stable than the TTM, which reduces the frequency
153 of motions of the platform. Second, the StableMoor platform is capable of supporting a bottom-
154 tracking acoustic Doppler profiler, which provides an independent measure of the platform's trans-
155 lational motion. Disadvantages of the StableMoor include: its size, which adds to the challenge of
156 deployment and recovery, and its cost, which is significantly higher than the TTM system.

157 *c. Turbulence Torpedo*

158 The turbulence torpedo is a simple sounding weight with an ADV head mounted forward of the
159 nose, and the ADV pressure case strapped below. This platform was deployed on May 14, 2015,
160 for 37 minutes starting at 07:41 local time. This measurement was made from a davit that hung
161 the system from the side of the ship to a depth of approximately 25 m. The primary logistical
162 advantages of this platform are its compact size, low cost, and the flexibility to perform spatial
163 transects.

164 *d. Coordinate system and turbulence averaging*

165 Unless stated otherwise, vector quantities in this work are in a fixed “principal-axes” coordinate
166 system that is aligned with the bidirectional tidal flow: positive u is in the direction of ebb (310°
167 True), positive w is vertically upward, and v is the cross-stream component in a right-handed
168 coordinate system. The full velocity vector, $\vec{u} = (\tilde{u}, \tilde{v}, \tilde{w})$, is separated into a mean and turbulent
169 component as $\vec{u} = \bar{\vec{u}} + \vec{u}$, where the over-bar denotes a 5-minute average. Turbulence kinetic
170 energy, $\text{tke} = \overline{u^2} + \overline{v^2} + \overline{w^2}$, and Reynold’s stresses, \overline{uv} , \overline{uw} , \overline{vw} , are computed by averaging over the
171 5-minute window. Throughout this work, we use $\bar{U} = (\bar{u}^2 + \bar{v}^2)^{1/2}$ to denote the mean horizontal
172 velocity magnitude.

173 All spectra, $S\{x\}(f) = |\mathcal{F}\{x(t)\}|^2$, and cross spectra, $C\{x, y\}(f) = \text{real}(\mathcal{F}\{x(t)\}\mathcal{F}\{y(t)\})$, are
174 computed using NumPy fast Fourier transform routines (van der Walt et al. 2011). Here, $\mathcal{F}\{x(t)\}$
175 denotes the fast Fourier transform of a signal $x(t)$. Time series, e.g., $x(t)$, are linearly detrended
176 and Hanning windowed prior to computing $\mathcal{F}\{x\}$ to reduce spectral reddening.

177 Throughout the remainder of this work, the dependence of S and C on f is implied (e.g., $S\{x\}(f)$
178 is hereafter $S\{x\}$), and for other variables the dependence on t is implied. Spectra and cross
179 spectra are normalized to preserve variance: $\int S\{u\}df = \overline{u^2}$, and $\int C\{u, v\}df = \overline{uv}$. The notations

180 $S\{\vec{u}\} = (S\{u\}, S\{v\}, S\{w\})$, and $C\{\vec{u}\} = (C\{u, v\}, C\{u, w\}, C\{v, w\})$ denote the set of spectra and
 181 cross spectra for each velocity component and pairs of components, respectively.

182 Turbulence dissipation rates are computed as:

$$\varepsilon = \frac{1}{U} \left(\alpha \left\langle (S\{u\} + S\{v\} + S\{w\}) f^{5/3} \right\rangle_{f_{IS}} \right)^{3/2} \quad (1)$$

183 Where $\alpha = 0.5$, and $\langle \rangle_{f_{IS}}$ denotes an average over the inertial subrange of the velocity spectra and
 184 where the signal-to-noise ratio is small (Lumley and Terray 1983; Sreenivasan 1995). Throughout
 185 this work, we take this average from 0.3 to 1 Hz for the u and v components, and 0.3 to 3 Hz for
 186 the w component.

187 3. Methodology

188 The essential approach of motion correction is to estimate the time series of velocity on a com-
 189 pliant mooring by obtaining an independent estimate of ADV head motion and removing that
 190 motion from the measured signal. Previous works have utilized inertial motion sensors to quantify
 191 the motion of multiscale profilers for the purpose of measuring the full spectrum of oceanic shear
 192 (Winkel et al. 1996). Nortek’s ADV-IMU measures the linear acceleration, \vec{a} , rotational motion,
 193 $\vec{\omega}$, and orientation matrix, \mathbf{R} , of the ADV pressure case (body) in the Earth reference frame. So
 194 long as the ADV head is rigidly connected to the ADV pressure case, it is possible to utilize the
 195 IMU motion signals to calculate the motion of the ADV head and remove it from the measured
 196 velocity signal. A similar approach has been used to correct sonic anemometer measurements of
 197 atmospheric turbulence (e.g., Miller et al. 2008). The ADV head motion is calculated as the sum
 198 of rotational and translational motion:

$$\begin{aligned} \vec{u}_h &= \vec{u}_\omega + \vec{u}_a + \vec{u}_{low} \\ &= \mathbf{R}^T \cdot \vec{\omega}^*(t) \times \vec{\ell}^* + \int \{\vec{a}(t)\}_{HP(f_a)} dt + \vec{u}_{low} \end{aligned} \quad (2)$$

Here, * superscripts denote quantities in the ADV's local coordinate system, and $\vec{\ell}^*$ is the vector from the IMU to the ADV head. \mathbf{R}^T —the inverse of the orientation matrix—rotates vectors from the IMU to the Earth reference frame. The notation $\{\vec{a}\}_{HP(f_a)}$ indicates that the IMU's accelerometer signal is high-pass filtered (in the Earth's stationary reference frame) at a chosen filter-frequency, f_a . This is necessary because accelerometers have low-frequency noise, sometimes referred to as bias-drift (Barshan and Durrant-Whyte 1995; Bevly 2004; Gulmammadov 2009).

Integrating \vec{a} to estimate \vec{u}_a amplifies the bias-drift noise at low frequencies, which dramatically reduces the signal-to-noise ratio at those time scales (Figure A1). The high-pass filtering reduces this noise so that it does not contaminate motion correction, but real motion that exists at these frequencies is still lost in the low signal-to-noise ratio (Egeland 2014; VanZwieten et al. 2015). This means that low-frequency motion is not well resolved by the IMU, and so there is a residual low-frequency translational motion, \vec{u}_{low} , that needs to be measured independently—or at the very least considered—when using motion-corrected ADV-IMU data. The $\vec{\omega}$ and \vec{u}_ω estimates do not have the same issue because there is no integration involved, and because low-frequency bias-drift in the $\vec{\omega}$ sensors is stabilized by the IMU's on-board Kalman filtering (i.e., the accelerometer and magnetometer signals provide estimates of down and north, respectively, which stabilize orientation estimates and eliminates bias from rotation estimates).

The choice of a high-pass filter for reducing low-frequency accelerometer noise depends on the flow conditions of the measurement and the platform being used. In particular, filter selection involves a trade-off between filtering out the bias-drift noise while not filtering out measured motion that is unresolved by an independent measurement of \vec{u}_{low} . If an independent measure of low-frequency motion is available it can be used to increase the accuracy of \vec{u}_h at low frequency. Note

that, to avoid double counting, \vec{u}_{low} should be estimated by applying the complementary low-pass filter to the independent measurement of low-frequency motion.

With this estimate of ADV head motion, it is straightforward to correct the measured velocity, \vec{u}_m , to estimate the velocity in the Earth’s inertial reference frame:

$$\vec{u}(t) = \vec{u}_m(t) + \vec{u}_h(t). \quad (3)$$

Note here that the ‘+’-sign is correct because head motion, \vec{u}_h , induces a measured velocity in the opposite direction of the head motion itself ($\vec{u}_m = \vec{u} - \vec{u}_h$).

For the TTM and turbulence torpedo, we utilize $f_a = 0.0333\text{Hz}$ (30-s period) and assume that $\vec{u}_{\text{low}} = 0$. For the StableMoor buoy, $f_a = 0.2\text{Hz}$ (5-s period). The bottom-track velocity was low-pass filtered at this frequency to provide an estimate of \vec{u}_{low} , and \vec{a} was high-pass filtered at this frequency. We use 4-pole, bidirectional (zero-phase), Hanning filters for all filtering operations.

Additional details on motion correction—including a detailed accounting of the distinct coordinate systems of the IMU, ADV pressure case, and ADV head—can be found in Kilcher et al. (2016). Open-source Python tools for performing motion correction of ADV-IMU data—including scripts that write processed data in Matlab and tabulated formats—are available at <http://lkilcher.github.io/dolfyn/>.

4. Results

a. Mean velocity

Figure 7 shows a comparison of \vec{u} measured by an ADV-IMU mounted on a TTM, to an upward-looking acoustic Doppler profiler mounted on the TTM anchor. This comparison shows excellent agreement between the ADV and Doppler profiler measurements of mean velocity. The \bar{u} , \bar{v} , and \bar{w} components have a root-mean-square error of 0.05, 0.13, and 0.03 m/s, respectively. Although

243 it is important to note that there is some discrepancy between ADP- and ADV-measured velocities
244 (especially in \bar{v} , which is most likely due to incomplete motion correction), the agreement between
245 the magnitude and direction of these independent velocity measurements indicates that moored
246 ADV-IMUs provide a reliable estimate of velocity in the Earth’s reference frame.

247 *b. TTM spectra*

248 As discussed in detail in Part 1, the mooring motion of the TTM, $S\{\vec{u}_h\}$, has a peak at 0.1 to 0.2
249 Hz from swaying of the mooring that is most likely driven by eddy shedding from the spherical
250 buoy (Figure 8, red lines). There is also higher-frequency broadband motion that is associated
251 with fluttering of the strongback fin around the mooring line. Both of these motions are especially
252 energetic in the v -component spectra because this is the direction in which the TTM mooring
253 system is most unstable. As is expected from fluid-structure interaction theory, the amplitude of
254 these motions increases with increasing mean velocity (Morison et al. 1950).

255 The mooring motion contaminates the uncorrected ADV measurements of velocity, $S\{\vec{u}_m\}$,
256 whenever the amplitude of the motion is similar to or greater than the amplitude of the turbulence.
257 Fortunately, much of this motion can be removed using the IMU’s motion signals as detailed in
258 Section 3. Lacking an independent measurement of turbulence velocity at this site, we interpret
259 the agreement of these spectra with turbulence theory as evidence of the success of the method.
260 In particular, at high frequencies ($f > 0.3$ Hz) for each mean-flow speed, the spectra decay with
261 a $f^{-5/3}$ slope and have equal amplitude across the velocity components. These results are con-
262 sistent with Kolmogorov’s (1941) theory of isotropic turbulence, and are consistent with spectral
263 shapes of earlier measurements of turbulence in energetic tidal channels from stationary platforms
264 (Walter et al. 2011; Thomson et al. 2012; McMillan et al. 2016).

For $|\vec{u}| > 1.0$, motion correction modifies the u and v component spectra at frequencies as high as 3 Hz. This outcome indicates that in order for motion correction to be effective, synchronization between the ADV and IMU needs to be within 1/3 s or better. This suggests that asynchronous approaches to motion correction may be challenging, especially considering that the clock drift of some instrumentation can be as high as a few seconds per day. By integrating the IMU data into the ADV data stream, the Nortek ADV-IMU achieves a synchronization to within 1e-2 s.

At low frequencies the spectra tend to become roughly constant (especially at higher flow speeds), which is also consistent with previous works. Note that the very low magnitude of $S\{\vec{u}_h\}$ at low frequencies is partially a result of filtering the IMU's accelerometer signal when calculating \vec{u}_a . The true low-frequency spectrum of ADV head motion is unknown (indicated using a dashed line below f_a). A comparison of $S\{\vec{u}\}$ measured by the TTM to that measured by the ADP—during the June 2012 deployment—reveals agreement at low frequencies (not shown). This finding suggests that the assumption that $\vec{u}_{low} = 0$ at these frequencies and at this site for this platform is justified—even if $S\{\vec{u}_h\}$ is not as low as indicated in Figure 8.

As successful as motion correction is, some of the motion contamination persists in $S\{\vec{u}\}$. This is most notable in $S\{v\}$ at the highest flow speeds (> 2.0 m/s): a peak at 0.15 Hz is an order of magnitude larger than a spectral fit to the other frequencies would indicate. This persistent motion contamination is evident to a lesser degree in $S\{u\}$ for $|u| > 2$ m/s, and in $S\{v\}$ at lower flow speeds. $S\{w\}$ appears to have no persistent motion contamination because the amplitude of the motion in this direction is much lower than for the other two components. For these measurements, $S\{w_h\}$ is so low that w -component motion correction makes only a minor correction to the spectra.

The amplitude of the persistent motion contamination peaks in $S\{v\}$ at 0.15 Hz is a factor of 5 to 10 times smaller than the amplitude of the ADV head motion itself. This observation suggests that the Microstrain IMU can be used to effectively correct mooring motion at 0.15 Hz when

the amplitude of that motion is less than 5 times the amplitude of the real turbulence spectrum. As a result, we have chosen a value of 3 as a conservative estimate of the motion correction's effectiveness.

In addition to the primary benefit of correcting for mooring motion, the IMU measurements can also be used to identify and screen out persistent motion contamination. For example, one of the most common uses of turbulence spectra is for the calculation of ε and τ_{ke} . For these purposes, and based on the relative amplitudes of the 0.15-Hz peaks, we assume that persistent motion contamination is likely, where $S\{\vec{u}_h\}/S\{\vec{u}\} > 3$, and thereby exclude these regions from spectral fits.

In the present case, for the u and w spectra, this criteria only excludes a narrow range of frequencies at the 0.15-Hz motion peak for some cases. This criteria is more restrictive of the v -component spectra at high frequencies for $\bar{U} > 1.0$ m/s, but this may be acceptable because the amplitude of $S\{v\}$ at these frequencies—i.e., in the isotropic inertial subrange—should be equal to that of $S\{u\}$ and $S\{w\}$ (Kolmogorov 1941).

Agreement of the v -component spectral amplitude with that of u and w at frequencies > 0.3 Hz indicates that motion correction is effective at those frequencies even when $S\{\vec{u}_h\}/S\{\vec{u}\} \gtrsim 3$. This outcome suggests that our screening threshold is excessively conservative at those frequencies, and that a more precise screening threshold may be frequency dependent. For example, it might take into account the f^3 character of the noise in $S\{\vec{u}_a\}$ (Figure A1). For the purpose of this work, the $S\{\vec{u}_h\}/S\{\vec{u}\} < 3$ threshold for spectral fits is sufficient, and detailed characterization of the IMU's motion- and frequency-dependent noise level is left for future work.

310 *c. StableMoor Spectra*

311 The spectra of the StableMoor motion has a broader peak with a maximum amplitude that is ap-
312 proximately half the frequency of the TTM spectral peak (Figure 9). The motion of this platform
313 also does not have high-frequency “subpeaks” or other high-frequency broadbanded excitation
314 (Part 1). These characteristics of the motion are most likely due to the more massive and hydro-
315 dynamically streamlined properties of the platform.

316 Like the TTM, the motion-corrected spectra from the StableMoor buoy are consistent with turbu-
317 lence theory and previous observations. Most importantly, there is an improvement in the quality
318 of the motion-corrected spectra compared to the TTM. In particular, the persistent motion con-
319 tamination peaks are completely removed. That is, this measurement system provides an accurate
320 estimate of the turbulence spectra at this location from low frequencies to more than 1 Hz—well
321 into the inertial subrange—for all three components of velocity.

322 Note that this level of accuracy cannot be obtained without the independent estimate of \vec{u}_{low} .
323 If we assume that $\vec{u}_{low} = 0$, a similar plot to Figure 9 (not shown) reveals persistent motion-
324 contamination peaks and troughs in the u and v spectra regardless of the choice of f_a . This as-
325 sumption indicates that the low-frequency motion of the StableMoor buoy is below a threshold in
326 which the IMU’s signal-to-noise ratio is high enough to resolve its motion. In other words, com-
327 pared to the TTM, the StableMoor platform provides a more accurate measurement of turbulence
328 when it includes an independent measure of \vec{u}_{low} (here a bottom-tracking ADCP), but it does no
329 better—and perhaps worse—when it does not.

330 *d. Torpedo spectra*

331 The u and v motion of the turbulence torpedo is broadbanded and the w motion has a narrow
332 peak at 0.3 Hz (Figure 10). Because \vec{u}_h is estimated using $f_a = 0.0333\text{Hz}$ and assuming $\vec{u}_{low} = 0$,

333 its spectra rolls off quickly below f_a . Motion correction of the torpedo data appears to effec-
 334 tively remove a motion peak from $S\{w\}$ at 0.3 Hz, and straightens out $S\{v\}$ between 0.04 and
 335 0.6 Hz. $S\{u\}$ is mostly unaffected by motion at these frequencies, because the torpedo motion
 336 is smaller than the turbulence in this direction. At frequencies below f_a , $S\{u\}$ and $S\{v\}$ increase
 337 dramatically. This increase suggests that unresolved, low-frequency motion of the torpedo is con-
 338 taminating the velocity measurements at these frequencies. It may be possible to correct for some
 339 of this contamination using a measurement of the ship's motion as a proxy for the torpedo's low-
 340 frequency motion, but this has not been done. Still, above f_a , the torpedo appears to provide a
 341 reliable estimate of spectral amplitude in the inertial subrange and can therefore be used to esti-
 342 mate ε . Considering the simplicity of the platform, it may be a useful option for quantifying this
 343 essential turbulence quantity in a variety of scenarios. Further, if a GPS is positioned above it, it
 344 may be capable of providing even more.

345 *e. Cross Spectra*

346 Inspection of cross spectra from TTM measurements demonstrates that motion correction can
 347 reduce motion contamination to produce reliable estimates of velocity cross spectra (Figure 11).
 348 At low flow speeds (left column), cross spectra between components of \vec{u}_h (i.e., between compo-
 349 nents of head motion, red) are small compared to correlated velocities. As the velocity magnitude
 350 increases (center and right columns), the swaying motion of the TTM at 0.15 Hz appears as a peak
 351 in the amplitude of the cross spectra of \vec{u}_h (red) and \vec{u}_m (black) for all three components of cross
 352 spectra (rows). Fortunately, motion correction reduces the amplitude of this peak dramatically so
 353 that $C\{\vec{u}\}$ (blue) is small at 0.15 Hz compared to lower frequencies. Furthermore, the fact that the
 354 standard deviation of $C\{\vec{u}\}$ is also relatively small at 0.15 Hz suggests that motion correction is
 355 effective for each spectral window, not just in their mean.

356 These results indicate that motion-corrected TTM velocity measurements can be used to obtain
357 reliable estimates of turbulence Reynold’s stresses, which are the integral of the cross spectra.
358 Without motion correction, Reynold’s stress estimates would be contaminated by the large peaks
359 in the cross spectra that are caused by the swaying and fluttering motion of the TTM vane.

360 A similar investigation of StableMoor cross spectra (not shown) indicates that cross-spectral
361 motion contamination is at a much lower amplitude than for the TTM. The low-frequency (< 0.3
362 Hz) “swimming” motion of that platform produces a minimal cross-spectral signal, and the relative
363 large mass of the platform minimizes the kinds of higher-frequency swaying and fluttering that
364 creates large values of cross-spectral head motion. Thus, the StableMoor platform also produces
365 reliable estimates of Reynold’s stresses, which are presumed to be improved by motion correction.

366 5. Discussion

367 The previous section presented a comparison of \vec{u} measured by a TTM-mounted ADV to mea-
368 surements from a co-located ADP. This comparison demonstrated that the IMU provides a reliable
369 estimate of the ADV’s orientation and that this can be utilized to estimate mean velocity in the
370 Earth’s reference frame. Turbulence velocity estimates from the same ADP are also in agree-
371 ment with low-frequency TTM turbulence estimates (not shown), but the ADP does not resolve
372 turbulence at the scales where motion contamination is strongest (0.1 to 1.0 Hz).

373 Ideally, moored motion-corrected turbulence velocity measurements would be validated against
374 simultaneous independent validated measurements of turbulence velocity at the same scales and
375 exact time and location. Accomplishing this, however, involves significant technical challenges
376 that are not easily overcome—most notably the difficulty of measuring turbulence at the same point
377 as the moving ADV. A slightly less ideal but much more realistic confirmation of the methodology
378 might involve comparing the statistics of moored turbulence measurements to those from a nearby

379 fixed platform, or a fixed platform placed at the same location at a different time (e.g., the “TTT”
380 platform described in Thomson et al. 2012). Unfortunately, to our knowledge, these measurements
381 have not yet been made.

382 Lacking a relevant, fixed, independent turbulence measurement to compare to it is instructive
383 to demonstrate the degree to which the moored measurements are consistent with turbulence
384 theory and other turbulence measurements in similar flow environments. The previous section
385 showed that the shape of the turbulence velocity spectra from moored ADVs is consistent with
386 Kolmogorov’s theory of locally isotropic turbulence, which has been observed consistently in tur-
387 bulence measurements for decades (Kolmogorov 1941; Grant et al. 1962; McMillan et al. 2016).
388 In particular, we observed an isotropic subrange—an $f^{-5/3}$ spectral slope and equal amplitude
389 spectra between components—that is driven by anisotropic turbulence at longer timescales (Fig-
390 ures 8, 9, 10). This finding is interpreted as the first indication that the measurement systems
391 presented are capable of accurately resolving turbulence. The degree to which uncorrected spec-
392 tra were corrected toward this theoretical and observationally confirmed shape is interpreted as a
393 measure of the improvement of the spectral estimates by motion correction.

394 Figure 12 presents a time series of the mean velocity (A) and several turbulence statistics that
395 were measured during the June 2014 TTM deployment. This figure shows the evolution of the flow
396 through Admiralty Inlet during 1.5 tidal cycles. The ϵ (B), Reynold’s stresses (C), dissipation,
397 and one component of turbulence production (D) grow and strengthen with ebb or flood then
398 subside during slack tide. This component of turbulence production is:

$$P_{uz} = \frac{\partial \bar{u}}{\partial z} \overline{uw} \quad . \quad (4)$$

399 Where $\partial \bar{u} / \partial z$ is computed from the two ADVs on the TTM. The highest values of ϵ and P_{uz} occur
400 at the peak of the ebb or flood, which is in agreement with other measurements in tidal channels.

401 The agreement of the magnitude of P_{uz} with ε at those times suggests a local production-dissipation
402 balance that is often observed in tidally forced channels (Trowbridge et al. 1999; Stacey et al.
403 1999b; McMillan et al. 2016). At other times, the value of P_{uz} is insufficient to balance ε or is
404 negative.

405 Inspection of the negative P_{uz} values reveals that most of them are caused by a reversed sign of \overline{uw}
406 rather than a reversed sign of $\partial u / \partial z$ (i.e., when compared to the sign of u). This finding suggests
407 that uncertainty in \overline{uw} may be contributing to discrepancies between P_{uz} and ε . Furthermore,
408 considering the complex nature of the shoreline near this site (i.e., the headland), it is not surprising
409 that P_{uz} does not balance ε perfectly. Other terms of the tke equation are likely to be important,
410 such as other components of production, advection terms, or turbulent transport terms. The fact
411 that these two terms are in near balance as often as they are is a strong indication that bottom
412 boundary layer physics are important to the dynamics at this site.

413 Figure 13 compares individual values of P_{uz} with ε directly. Given the assumptions implicit in
414 this comparison and the discussion above, the agreement between P_{uz} and ε is an encouraging
415 result that suggests the turbulent boundary reaches the depth of these measurements (10 m) during
416 the highest flow speeds. This result is further supported by a comparison of \bar{U} with ε (Figure
417 14). Here we see a $\varepsilon \propto \bar{U}^3$ dependence that is again suggestive of bottom boundary layer physics
418 (Trowbridge 1992; Nash et al. 2009). At lower flow speeds, ε deviates from this relationship,
419 which suggests that the boundary layer is no longer the dominant physical process at the depth of
420 these measurements.

421 6. Conclusion

422 This work presents a methodology for measuring turbulence from moored ADV-IMUs and de-
423 tails an approach for removing the IMU-measured mooring motion from the ADV's velocity mea-

424 surements. The IMU integrated into the Nortek Vector ADV has been configured to provide esti-
425 mates of the ADV’s orientation and motion at every time step of the ADV’s sampling. The tight
426 integration of the IMU and ADV data streams provides a data set that can be used to correct ve-
427 locity measurements for mooring motion and rotate those measurements into the Earth’s reference
428 frame.

429 Comparison of spectra of ADV head motion, $S\{\vec{u}_h\}$, to that of motion-corrected, $S\{\vec{u}\}$, and
430 uncorrected spectra, $S\{\vec{u}_m\}$, reveals that motion correction improves spectral estimates of moored
431 ADV measurements. In particular, we found that motion-corrected spectra have spectral shapes
432 that are similar to previous measurements of tidal-channel turbulence and have a $f^{-5/3}$ spectral
433 slope at high frequencies. This finding suggests that the motion-corrected spectra resolve the
434 inertial subrange predicted by Kolmogorov’s theory of locally isotropic turbulence.

435 Motion correction reduces motion contamination for all platforms we presented but it does not
436 necessarily remove it completely. This outcome seems to depend on the relative amplitude of
437 platform motion compared to the underlying turbulence being measured. The most notable ex-
438 ample of this is from the TTM, which has a large “swaying” peak at 0.1 Hz. Where this peak
439 is very large—especially in the v component—it is not reduced to a level that is consistent with
440 earlier measurements of tidal-channel turbulence—i.e., there is no smooth roll-off between the
441 low-frequency energy-containing scales and the $f^{-5/3}$ inertial subrange.

442 This inconsistency indicates that turbulence measurements from moored, motion-corrected IMU
443 ADVs must be interpreted with care. An inspection of spectra presented here suggests that exclud-
444 ing spectral regions where $S\{\vec{u}_h\}/S\{\vec{u}\} > 3$ removes persistent-motion contamination peaks while
445 still preserving spectral regions where motion correction is effective. Using this criteria, it is then
446 possible to produce spectral fits that exclude persistent-motion contamination, and provide reliable
447 estimates of turbulence quantities of interest (e.g., ϵ and tke).

448 We've also shown that motion correction reduces motion contamination in cross spectra. This
449 finding is important because it suggests that moored IMU-ADV measurements may be used to
450 produce reliable estimates of Reynolds stresses. We utilized these stress estimates and vertical
451 shear estimates, both from the TTM, to estimate P_{uz} .

452 Finally, we have shown that ε estimates based on motion-corrected spectra scale with the U^3 , and
453 balance P_{uz} estimates during ebb and flood. Together, these results indicate that bottom boundary
454 layer physics are a dominant process at this site, and that the boundary layer reaches the height
455 of the IMU ADVs (10 m) during ebb and flood. The degree of agreement between P_{uz} and ε also
456 serves as an indicator of the self-consistency of moored IMU-ADV turbulence measurements.

457 *Acknowledgments.* Many thanks to Joe Talbert, Alex DeKlerk, Captain Andy Reay-Ellers, Jen-
458 nifer Rinker, Maricarmen Guerra, and Eric Nelson in assisting with data collection. The authors
459 are also grateful to James VanZwieten, Matthew Egeland and Marshall Richmond for discussion
460 on the details of this work.

461 This work was supported by the U.S. Department of Energy under Contract No. DE-AC36-
462 08GO28308 with the National Renewable Energy Laboratory. Funding for the work was provided
463 by the DOE Office of Energy Efficiency and Renewable Energy, Wind and Water Power Technolo-
464 gies Office.

465 The U.S. Government retains and the publisher, by accepting the article for publication, ac-
466 knowledges that the U.S. Government retains a nonexclusive, paid-up, irrevocable, worldwide
467 license to publish or reproduce the published form of this work, or allow others to do so, for U.S.
468 Government purposes.

A1. Comparing StableMoor \vec{u}_{low} to IMU \vec{u}_{h}

To better understand the IMU’s signal-to-noise ratio, we compare the motion of the StableMoor buoy from the ADP bottom track measurements, \vec{u}_{BT} , to the IMU’s estimates of ADP motion. To do this, we compute the IMU’s estimate of ADP motion using equation (2), and replacing ℓ^* with the vector that points from the IMU to the ADP head. We then linearly interpolate the ADP measurements of \vec{u}_{BT} onto the times of the ADV-IMU measurements.

The coherence between these two signals is high and statistically significant over 1.5 decades—from 0.03 to 0.8 Hz (Priestley 1981). The v component has the highest coherence, 98%, because this is the direction that has the most motion (i.e., these estimates have a higher signal-to-noise ratio). The u and w components have a slightly lower coherence, 80% and 65%, respectively.

On the low-frequency side, our interpretation is that the signal-to-noise ratio of the IMU increases dramatically below 0.03 Hz, resulting in low coherence. On the high-frequency side, Doppler noise in the ADP measurements contaminates its estimates of motion, causing the decrease in coherence at 0.8 Hz. A comparison of the phase between these signals shows that there is no lag between the measurements (not shown).

These results help to inform the selection of zero-lag filters used to estimate \vec{u}_{low} from \vec{u}_{BT} . In particular, by selecting 0.2 Hz, we target the middle of the coherence peak between the two measurements. Furthermore, the rapid decrease in coherence below 0.03 Hz provides an objective measurement of the frequency at which IMU measured velocity becomes unreliable in the flow conditions we observed.

References

- Afgan, I., J. McNaughton, S. Rolfo, D. Apsley, T. Stallard, and P. Stansby, 2013: Turbulent flow and loading on a tidal stream turbine by les and rans. *International Journal of Heat and Fluid Flow*, **43**, 96–108.
- Alexander, S. R., and P. E. Hamlington, 2015: Analysis of turbulent bending moments in tidal current boundary layers. *Journal of Renewable and Sustainable Energy*, **7** (6), 063 118.
- Alford, M. H., 2010: Sustained, full-water-column observations of internal waves and mixing near mendocino escarpment. *Journal of Physical Oceanography*, **40** (12), 2643–2660, doi:10.1175/2010JPO4502.1.
- Bachmann, E. R., X. Yun, D. McKinney, R. B. McGhee, and M. J. Zyda, 2003: Design and implementation of MARG sensors for 3-DOF orientation measurement of rigid bodies. *International Conference on Robotics & Automation*, Taipei, Taiwan.
- Barshan, B., and H. F. Durrant-Whyte, 1995: Inertial navigation systems for mobile robots. *IEEE Transactions on Robotics and Automation*, **11** (3), 328–342.
- Bevly, D. M., 2004: Global positioning system (gps): A low-cost velocity sensor for correcting inertial sensor errors on ground vehicles. *Journal of dynamic systems, measurement, and control*, **126** (2), 255–264.
- Cartwright, G. M., C. T. Friedrichs, P. J. Dickhudt, T. Gass, and F. H. Farmer, 2009: Using the acoustic doppler velocimeter (adv) in the mudbed real-time observing system. *Marine Technology for Our Future: Global and Local Challenges*.
- Doherty, K., D. Frye, S. Liberatore, and J. Toole, 1999: A moored profiling instrument*. *Journal of Atmospheric and Oceanic Technology*, **16** (11), 1816–1829.

512 Egeland, M. N., 2014: Spectral evaluation of motion compensated ADV systems for ocean turbu-
 513 lence measurements. Ph.D. thesis, Florida Atlantic University.

514 Fer, I., and M. B. Paskyabi, 2014: Autonomous ocean turbulence measurements using shear probes
 515 on a moored instrument. *Journal of Atmospheric and Oceanic Technology*, **31** (2), 474–490, doi:
 516 10.1175/JTECH-D-13-00096.1.

517 Finlayson, D., 2005: Combined bathymetry and topography of the Puget Lowlands, Washington
 518 state. URL <http://www.ocean.washington.edu/data/pugetsound/>.

519 Geyer, R. W., M. E. Scully, and D. K. Ralston, 2008: Quantifying vertical mixing in estuaries.
 520 *Environmental Fluid Mechanics*, **8**, 495–509, doi:10.1007/s10652-008-9107-2.

521 Goodman, L., E. R. Levine, and R. G. Lueck, 2006: On measuring the terms of the turbulent
 522 kinetic energy budget from an auv. *Journal of Atmospheric and Oceanic Technology*, **23** (7),
 523 977–990, doi:10.1175/JTECH1889.1.

524 Grant, H. L., R. W. Stewart, and A. Moilliet, 1962: Turbulence spectra from a tidal channel.
 525 *Journal of Fluid Mechanics*, **12**, 241–263.

526 Gulmammadov, F., 2009: Analysis, modeling and compensation of bias drift in mems inertial
 527 sensors. *Recent Advances in Space Technologies, 2009. RAST'09. 4th International Conference*
 528 *on*, IEEE, 591–596.

529 Gunawan, B., V. S. Neary, and J. Colby, 2014: Tidal energy site resource assessment in the East
 530 River tidal strait, near Roosevelt Island, New York, NY (USA). *Renewable Energy*, **71**, 509–
 531 517, doi:10.1016/j.renene.2014.06.002.

Hand, M. M., N. D. Kelley, and M. J. Balas, 2003: Identification of wind turbine response to turbulent inflow structures. Tech. Rep. NREL/CP-500-33465, National Renewable Energy Laboratory.

Harding, S., L. Kilcher, and J. Thomson, 2017: Turbulence measurements from compliant moorings - part 1: Motion characterization, in review.

Kelley, N. D., B. J. Jonkman, G. N. Scott, J. T. Bialasiewicz, and L. S. Redmond, 2005: The impact of coherent turbulence on wind turbine aeroelastic response and its simulation. *WindPower*, Denver, Colorado, NREL/CP-500-38074, may 15-18.

Kilcher, L., J. Thomson, J. Talbert, and A. DeKlerk, 2016: Measuring turbulence from moored acoustic Doppler velocimeters: A manual to quantifying inflow at tidal energy sites. 9 62979, National Renewable Energy Laboratory. URL www.nrel.gov/docs/fy16osti/62979.pdf.

Kim, S. C., C. T. Friedrichs, J. P.-Y. Maa, and L. D. Wright, 2000: Estimating bottom stress in tidal boundary layer from acoustic doppler velocimeter data. *Journal of Hydraulic Engineering*, 399–406.

Kolmogorov, A. N., 1941: Dissipation of energy in the locally isotropic turbulence. *Dokl. Akad. Nauk SSSR*, **32** (1), 16–18, URL <http://www.jstor.org/stable/51981>.

Kraus, C., A. Lohrmann, and R. Cabrera, 1994: A new acoustic meter for measuring 3d laboratory flows. *Journal of Hydraulic Engineering*, **120**, 406–412.

Lohrmann, A., R. Cabrera, G. Gelfenbaum, and J. Haines, 1995: Direct measurements of reynolds stress with an acoustic doppler velocimeter. *Current Measurement, 1995., Proceedings of the IEEE Fifth Working Conference on*, 205–210, doi:10.1109/CCM.1995.516175.

553 Lorke, A., 2007: Boundary mixing in the thermocline of a large lake. *Journal of Geophysical*
554 *Research: Oceans*, **112** (C9), n/a–n/a, doi:10.1029/2006JC004008, c09019.

555 Lueck, R. G., and D. Huang, 1999: Dissipation measurement with a moored instrument in a swift
556 tidal channel. *Journal of atmospheric and oceanic technology*, **16**, 1499–1505.

557 Lumley, J., and E. Terray, 1983: Kinematics of turbulence convected by a random wave field.
558 *Journal of Physical Oceanography*, **13** (11), 2000–2007.

559 Marins, J. L., X. Yun, E. R. Bachmann, R. B. McGhee, and M. J. Zyda, 2001: An extended Kalman
560 filter for quaternion-based orientation estimation using MARG sensors. *International conference*
561 *on intelligent robots and systems*.

562 McCaffrey, K., B. Fox-Kemper, P. E. Hamlington, and J. Thomson, 2015: Characterization of
563 turbulence anisotropy, coherence, and intermittency at a prospective tidal energy site: Observa-
564 tional data analysis. *Renewable Energy*, **76**, 441–453.

565 McMillan, J. M., A. E. Hay, R. G. Lueck, and F. Wolk, 2016: Rates of dissipation of turbulent
566 kinetic energy in a high reynolds number tidal channel. *Journal of Atmospheric and Oceanic*
567 *Technology*, **33** (4), 817–837, doi:10.1175/JTECH-D-15-0167.1.

568 MicroStrain, I., 2010: Technical note: Coning and sculling. Tech. Rep. I0019, MicroStrain. URL
569 http://files.microstrain.com/TN-I0019_3DM-GX3-25__Coning_And_Sculling.pdf.

570 MicroStrain, I., 2012: *3DM-GX3-15,-25 MIP Data Communications Protocol*. URL [http:](http://files.microstrain.com/3DM-GX3-15-25-MIP-Data-Communications-Protocol.pdf)
571 [//files.microstrain.com/3DM-GX3-15-25-MIP-Data-Communications-Protocol.pdf](http://files.microstrain.com/3DM-GX3-15-25-MIP-Data-Communications-Protocol.pdf), retrieved
572 January 2014.

573 Miller, S. D., T. S. Hristov, J. B. Edson, and C. A. Friehe, 2008: Platform motion effects on
 574 measurements of turbulence and air-sea exchange over the open ocean. *Journal of Atmospheric
 575 and Oceanic Technology*, **25** (9), 1683–1694, doi:10.1175/2008JTECHO547.1.

576 Morison, J. R., J. W. Johnson, and S. A. Schaaf, 1950: The force exerted by surface waves on
 577 piles. *Journal of Petroleum Technology*, **2** (05), 149–154.

578 Moum, J., and J. Nash, 2009: Mixing measurements on an equatorial ocean mooring. *Journal of
 579 Atmospheric and Oceanic Technology*, **26** (2), 317–336.

580 Mücke, T., D. Kleinhans, and J. Peinke, 2011: Atmospheric turbulence and its influence on the
 581 alternating loads on wind turbines. *Wind Energy*, **14**, 301–316.

582 Nash, J. D., L. F. Kilcher, and J. N. Moum, 2009: Structure and composition of a strongly
 583 stratified, tidally pulsed river plume. *Journal of Geophysical Research*, **114**, C00B12, doi:
 584 10.1029/2008JC005036.

585 Nash, J. D., E. Kunze, J. M. Toole, and R. W. Schmitt, 2004: Internal tide reflection and turbulent
 586 mixing on the continental slope. *Journal of Physical Oceanography*, **34** (5), 1117–1134, doi:
 587 10.1175/1520-0485(2004)034<1117:ITRATM>2.0.CO;2.

588 Nortek, 2005: *Vector Current Meter User Manual*. Vangkroken 2, NO-1351 RUD, Norway, h ed.

589 Paskyabi, M. B., and I. Fer, 2013: Turbulence measurements in shallow water from a subsurface
 590 moored moving platform. *Energy Procedia*, **35**, 307 – 316, doi:10.1016/j.egypro.2013.07.183.

591 Polagye, B., and J. Thomson, 2013: Tidal energy resource characterization: methodology and field
 592 study in admiralty inlet, Puget Sound, WA (USA). *Proceedings of the Institution of Mechanical
 593 Engineers, Part A: Journal of Power and Energy*, **227** (3), 352–367.

594 Priestley, M., 1981: *Spectral Analysis and Time Series*. Academic Press, London.

595 Rippeth, T. P., E. Williams, and J. H. Simpson, 2002: Reynolds stress and turbulent en-
 596 ergy production in a tidal channel. *Journal of Physical Oceanography*, **32**, 1242–1251, doi:
 597 10.1175/1520-0485(2002)032\$(<\$1242:RSATEP\$>\$2.0.CO;2.

598 Sreenivasan, K. R., 1995: On the universality of the Kolmogorov constant. *Physics of Fluids*, **7**,
 599 2778–2784.

600 Stacey, M. T., S. G. Monismith, and J. R. Burau, 1999a: Measurements of reynolds stress
 601 profiles in unstratified tidal flow. *J. Geophys. Res.*, **104 (C5)**, 10 933–10 949, doi:10.1029/
 602 1998JC900095.

603 Stacey, M. T., S. G. Monismith, and J. R. Burau, 1999b: Observations of turbulence in a partially
 604 stratified estuary. *Journal of Physical Oceanography*, **29**, 1950–1970.

605 Thomson, J., B. Polagye, V. Durgesh, and M. Richmond, 2012: Measurements of turbulence at
 606 two tidal energy sites in Puget Sound, WA. *Journal of Oceanic Engineering*, **37 (3)**, 363–374,
 607 doi:10.1109/JOE.2012.2191656.

608 Trowbridge, J. H., 1992: A simple description of the deepening and structure of a stably stratified
 609 flow driven by a surface stress. *Journal of Geophysical Research*, **97**, 15 529–15 543.

610 Trowbridge, J. H., W. R. Geyer, M. M. Bowen, and A. J. I. Williams, 1999: Near-bottom turbu-
 611 lence measurements in a partially mixed estuary: turbulent energy balance, velocity structure
 612 and along-channel momentum balance. *Journal of Physical Oceanography*, **29**, 3056–3072.

613 van der Walt, S., S. C. Colbert, and G. Varoquaux, 2011: The numpy array: A structure for efficient
 614 numerical computation. *Computing in Science & Engineering*, **13**, 22–30, doi:10.1109/MCSE.
 615 2011.37.

616 VanZwieten, J. H., M. N. Egeland, K. D. von Ellenrieder, J. W. Lovenbury, and L. Kilcher, 2015:
 617 Experimental evaluation of motion compensated adv measurements for in-stream hydrokinetic
 618 applications. *Current, Waves and Turbulence Measurement (CWTM)*, 2015 IEEE/OES Eleventh,
 619 1–8, doi:10.1109/CWTM.2015.7098119.

620 Voulgaris, G., and J. H. Trowbridge, 1998: Evaluation of the acoustic doppler velocimeter (adv)
 621 for turbulence measurements. *Journal of Atmospheric and Oceanic technology*, **15**, 272–289.

622 Walter, R. K., N. J. Nidzieko, and S. G. Monismith, 2011: Similarity scaling of turbulence spectra
 623 and cospectra in a shallow tidal flow. *Journal of Geophysical Research: Oceans*, **116** (C10).

624 Wiles, P. J., T. P. Rippeth, J. H. Simpson, and P. J. Hendricks, 2006: A novel technique for
 625 measuring the rate of turbulent dissipation in the marine environment. *Geophysical Research*
 626 *Letters*, **33**, 21 608.

627 Winkel, D., M. Gregg, and T. Sanford, 1996: Resolving oceanic shear and velocity with the multi-
 628 scale profiler. *Journal of Atmospheric and Oceanic Technology*, **13** (5), 1046–1072.

629 Wyngaard, J. C., L. Rockwell, and C. A. Friehe, 1985: Errors in the measurement of turbulence
 630 upstream of an axisymmetric body. *Journal of Atmospheric and Oceanic Technology*, **2** (4),
 631 605–614.

632 Zhang, Y., K. Streitlien, J. G. Bellingham, and A. B. Baggeroer, 2001: Acoustic doppler ve-
 633 locimeter flow measurement from an autonomous underwater vehicle with applications to deep
 634 ocean convection. *Journal of Atmospheric and Oceanic Technology*, **18** (12), 2038–2051, doi:
 635 10.1175/1520-0426(2001)018<2038:ADVFMF>2.0.CO;2.

LIST OF FIGURES

Fig. 1.	Bathymetry of Admiralty Inlet near Port Townsend, Washington, U.S.A. (Finlayson 2005). The red dot indicates the location of all measurements. The positive u direction is the direction of ebb flow (thick arrow originating from red dot), and positive v is away from Admiralty Head (smaller arrow).	33
Fig. 2.	Schematic diagram of the TTM; not to scale.	34
Fig. 3.	TTM components on the deck of the R/V Jack Robertson. The TTM includes two ADVs, with pressure cases mounted on opposite sides of the fin. The anchor stack includes a pop-up buoy for retrieval. The green arrow indicates the vector from the IMU to the ADV head (face of the transmit transducer).	35
Fig. 4.	Top: Alex DeKlerk checks to ensure that the StableMoor buoy is properly fastened to its anchor; the RDI workhorse ADCP can be seen in the rear instrument bay. A bridle is draped across the top of the buoy for deployment and recovery, and a small marker buoy fastened to the tail is useful during recovery. Bottom: a close-up of the StableMoor with the ADV head and the top of its pressure case. The green arrow indicates the vector from the IMU to the ADV head.	36
Fig. 5.	The turbulence platform showing details of the ADV head and pressure case configuration. The green arrow indicates the vector from the IMU to the ADV head. The head cable was taped out of the way beneath the sounding weight tail fins shortly after taking this photo.	37
Fig. 6.	Spectra of \vec{u}_ω (yellow) and \vec{u}_a signals from the Microstrain IMU sitting on a motionless table. The \vec{u}_a signals are unfiltered (black), and high-pass filtered at 30 s (magenta), 10 s (blue), 5 s (green). Vertical dotted lines indicate the filter frequency. The black horizontal dotted line indicates the noise level of a Nortek Vector ADV configured to measure $\pm 4\text{m/s}$. The shaded region indicates the range of spectra presented herein ($0.002 < \text{tke} < 0.03 \text{ m}^2/\text{s}^2$, $1\text{e-}5 < \varepsilon < 5\text{e-}4 \text{ W/kg}$).	38
Fig. 7.	Time series of tidal velocity at Admiralty Head from TTM measurements (black), and an acoustic Doppler profiler (red). The profiler measurements—taken at the same depth as the ADV on the TTM—were contaminated by acoustic reflection from the strongback fin when it was inline with one of the profiler’s beams. Note that the vertical scale on the three axes vary by more than an order of magnitude; the small ticks in A and B are equivalent to the ticks in C.	39
Fig. 8.	Turbulence spectra from the June 2014 TTM deployment. Each column is for a range of streamwise velocity magnitudes (indicated at top). The rows are for each component of velocity (indicated to the lower right of the right column). The uncorrected spectra are in black and the corrected spectra are blue, and the spectra of ADV head motion, \vec{u}_h , is red (also indicated in the legend). The vertical red dotted line indicates the filter frequency applied to the IMU accelerometers when estimating \vec{u}_h ; below this frequency $S\{\vec{u}_h\}$ is plotted as a dashed line. Diagonal black dotted lines indicate a $f^{-5/3}$ slope. The number of spectral ensembles, N , in each column is indicated in the top row.	40
Fig. 9.	Turbulence spectra from the StableMoor buoy. The axes layout and annotations are identical to Figure 8, except that $S\{\vec{u}_h\}$ is plotted as a solid line at all frequencies because it is measured at all frequencies.	41

678	Fig. 10.	Turbulence spectra from the turbulence torpedo during a 35-minute period when the mean velocity was 1.3 m/s. Annotations and line colors are identical to Figure 8.	42
679			
680	Fig. 11.	The real part of the cross-spectral density between velocity components measured by the TTM. The upper row is the u - v cross-spectral density, the middle row is the u - w cross-spectral density, and the bottom row is the v - w cross-spectral density. The columns are for different ranges of the stream-wise mean velocity magnitude (indicated above the top row). The blue line is the cross spectrum between components of motion-corrected velocity, the red line is the cross spectrum between components of head-motion, and the black line is the cross spectrum between components of uncorrected velocity. The light blue shading indicates one standard deviation of the C for the motion-corrected cross-spectral density. N is the number of spectral ensembles in each column. The number in the lower-right corner of each panel is the motion-corrected Reynold's stress (integral of the blue line) in units of $1\text{e-}4 \text{ m}^2\text{s}^{-2}$	43
681			
682			
683			
684			
685			
686			
687			
688			
689			
690			
691	Fig. 12.	Time series of mean velocities (A), turbulence energy and its components (B), Reynold's stresses (C), and turbulence dissipation rate (D) measured by the TTM during the June 2014 deployment. Shading indicates periods of ebb ($\bar{u} > 1.0$, grey) and flood ($\bar{u} < -1.0$, lighter grey).	44
692			
693			
694			
695	Fig. 13.	$P_{u\bar{z}}$ vs. ε during the June 2014 TTM deployment for values of $ u > 1$ m/s. Values of negative production are indicated as open circles.	45
696			
697	Fig. 14.	A log-log plot of ε versus \bar{U} for the June 2014 TTM (diamonds) and May 2015 StableMoor (dots) deployments, during ebb (left) and flood (right). Black points are 5-minute averages. Green dots are mean values within speed bins of 0.2 m s^{-1} width that have at least 10 points (50 minutes of data); their vertical bars are 95% bootstrap confidence intervals. The blue line shows a U^3 slope, wherein the proportionality constant (blue box) is calculated by taking the log-space mean of ε/U^3	46
698			
699			
700			
701			
702			
703	Fig. 15.	Coherence between IMU-measured motion of StableMoor buoy and ADP bottom-track velocity for $1.0 < \bar{U} < 1.5$. The horizontal dotted line indicates the 95% confidence level for the 102 spectral windows in this estimate.	47
704			
705			

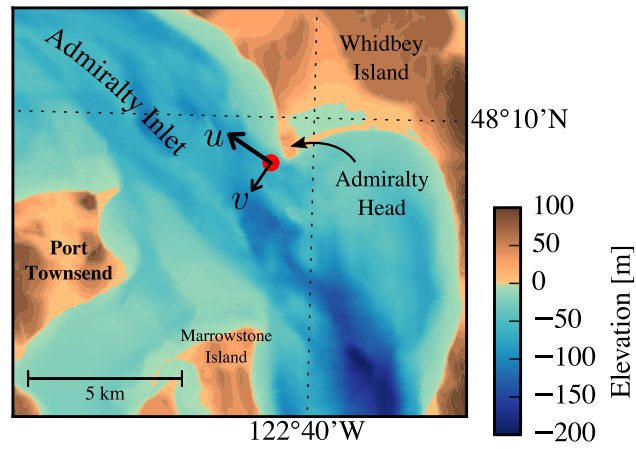


FIG. 1. Bathymetry of Admiralty Inlet near Port Townsend, Washington, U.S.A. (Finlayson 2005). The red dot indicates the location of all measurements. The positive u direction is the direction of ebb flow (thick arrow originating from red dot), and positive v is away from Admiralty Head (smaller arrow).

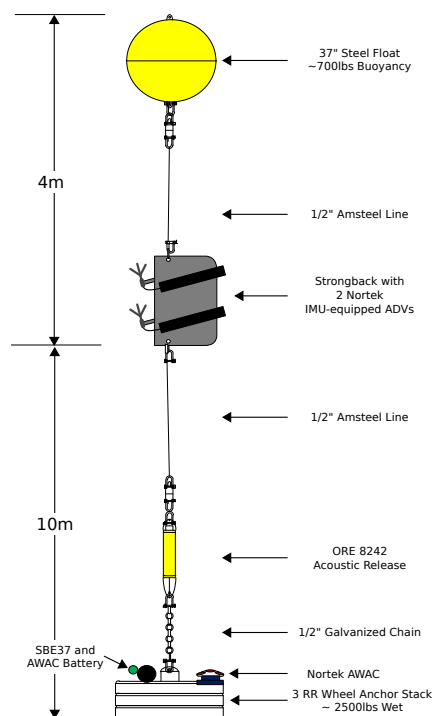
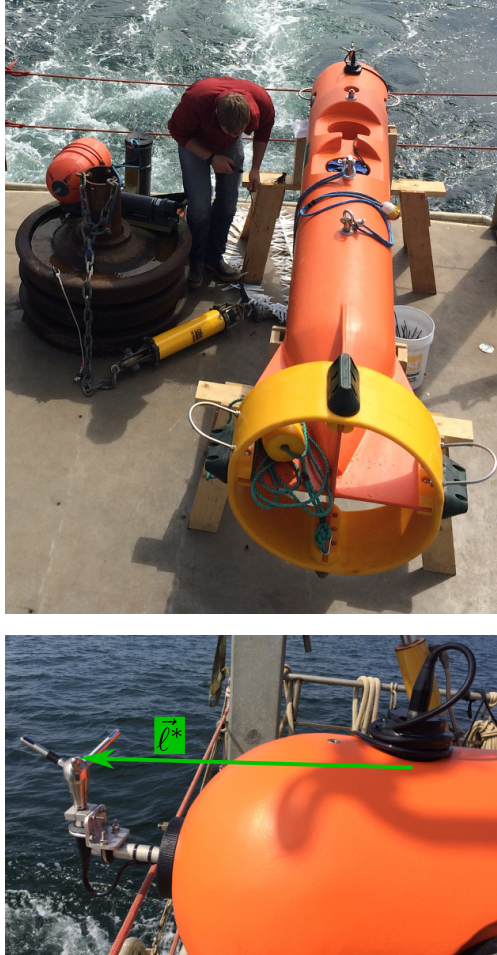


FIG. 2. Schematic diagram of the TTM; not to scale.



709 FIG. 3. TTM components on the deck of the R/V Jack Robertson. The TTM includes two ADVs, with
 710 pressure cases mounted on opposite sides of the fin. The anchor stack includes a pop-up buoy for retrieval. The
 711 green arrow indicates the vector from the IMU to the ADV head (face of the transmit transducer).



712 FIG. 4. Top: Alex DeKlerk checks to ensure that the StableMoor buoy is properly fastened to its anchor; the
 713 RDI workhorse ADCP can be seen in the rear instrument bay. A bridle is draped across the top of the buoy
 714 for deployment and recovery, and a small marker buoy fastened to the tail is useful during recovery. Bottom: a
 715 close-up of the StableMoor with the ADV head and the top of its pressure case. The green arrow indicates the
 716 vector from the IMU to the ADV head.



717 FIG. 5. The turbulence platform showing details of the ADV head and pressure case configuration. The green
718 arrow indicates the vector from the IMU to the ADV head. The head cable was taped out of the way beneath the
719 sounding weight tail fins shortly after taking this photo.

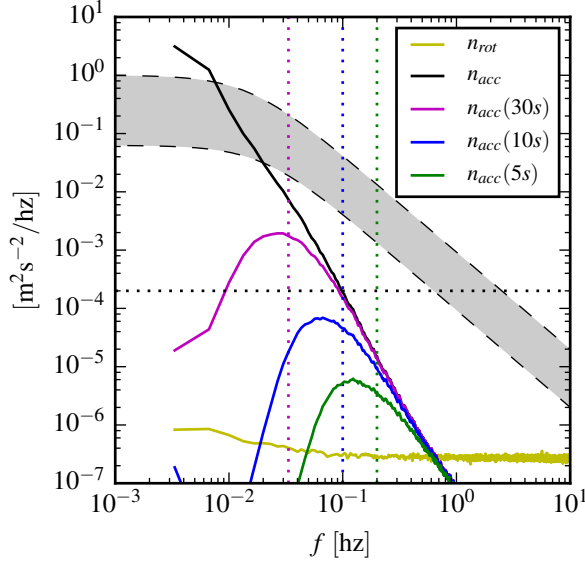
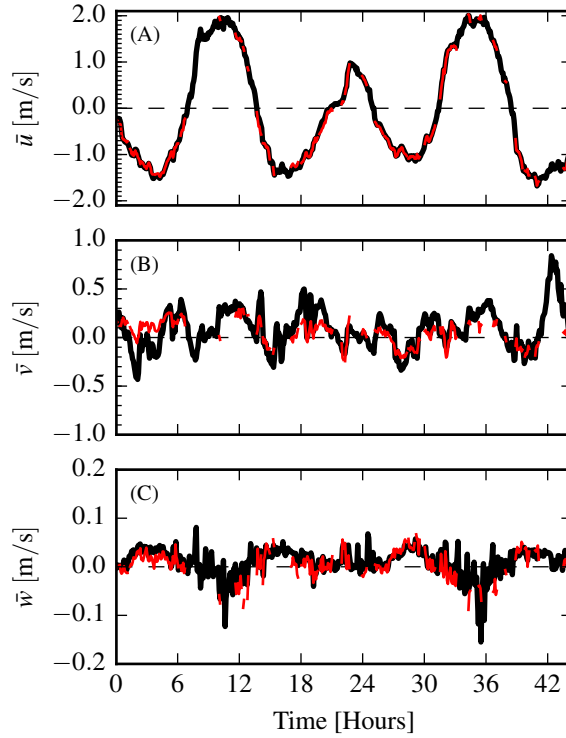


FIG. 6. Spectra of \vec{u}_ω (yellow) and \vec{u}_a signals from the Microstrain IMU sitting on a motionless table. The \vec{u}_a signals are unfiltered (black), and high-pass filtered at 30 s (magenta), 10 s (blue), 5 s (green). Vertical dotted lines indicate the filter frequency. The black horizontal dotted line indicates the noise level of a Nortek Vector ADV configured to measure $\pm 4\text{m/s}$. The shaded region indicates the range of spectra presented herein ($0.002 < \text{tke} < 0.03 \text{ m}^2/\text{s}^2$, $1\text{e-}5 < \varepsilon < 5\text{e-}4 \text{ W/kg}$).



725 FIG. 7. Time series of tidal velocity at Admiralty Head from TTM measurements (black), and an acoustic
 726 Doppler profiler (red). The profiler measurements—taken at the same depth as the ADV on the TTM—were
 727 contaminated by acoustic reflection from the strongback fin when it was inline with one of the profiler’s beams.
 728 Note that the vertical scale on the three axes vary by more than an order of magnitude; the small ticks in A and
 729 B are equivalent to the ticks in C.

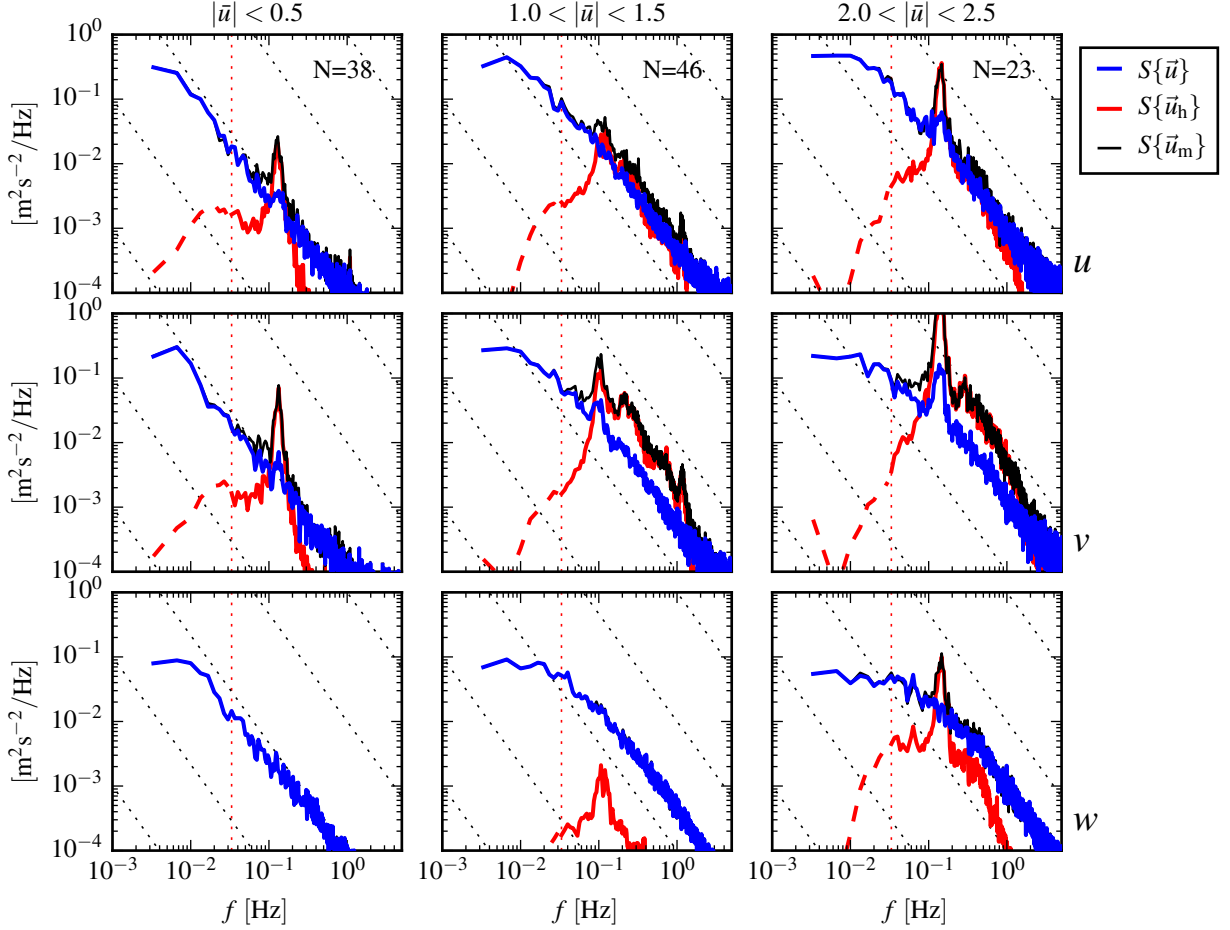


FIG. 8. Turbulence spectra from the June 2014 TTM deployment. Each column is for a range of streamwise velocity magnitudes (indicated at top). The rows are for each component of velocity (indicated to the lower right of the right column). The uncorrected spectra are in black and the corrected spectra are blue, and the spectra of ADV head motion, \vec{u}_h , is red (also indicated in the legend). The vertical red dotted line indicates the filter frequency applied to the IMU accelerometers when estimating \vec{u}_h ; below this frequency $S\{\vec{u}_h\}$ is plotted as a dashed line. Diagonal black dotted lines indicate a $f^{-5/3}$ slope. The number of spectral ensembles, N , in each column is indicated in the top row.

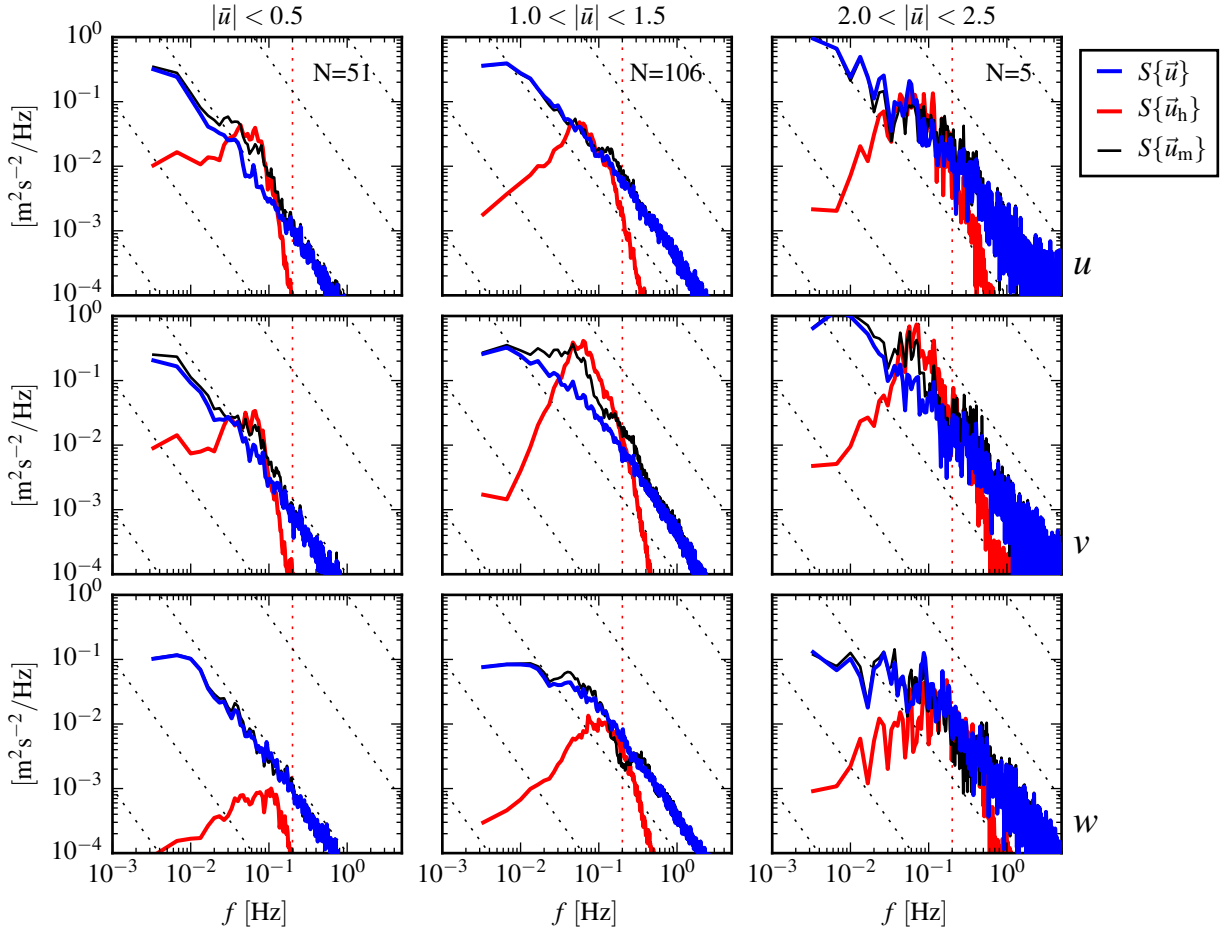


FIG. 9. Turbulence spectra from the StableMoor buoy. The axes layout and annotations are identical to Figure 8, except that $S\{\vec{u}_h\}$ is plotted as a solid line at all frequencies because it is measured at all frequencies.

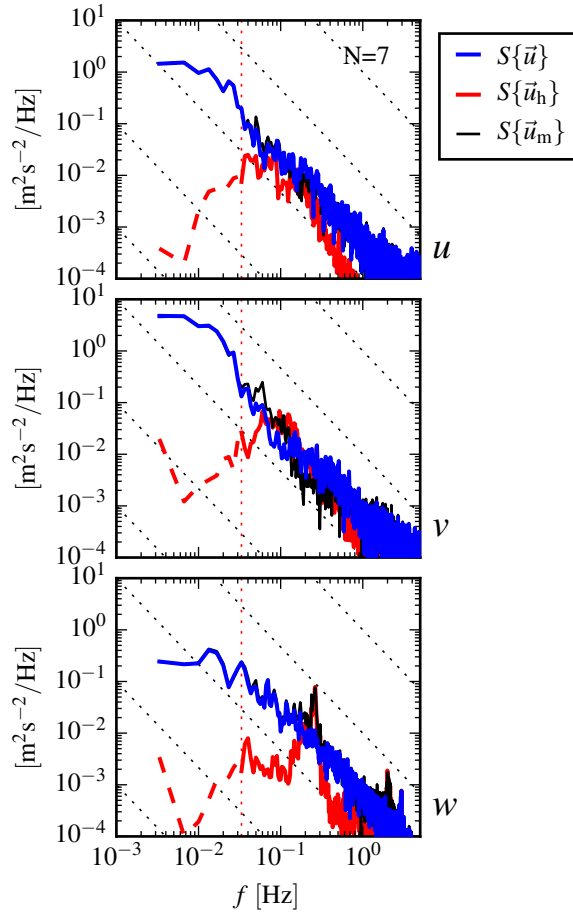


FIG. 10. Turbulence spectra from the turbulence torpedo during a 35-minute period when the mean velocity was 1.3 m/s. Annotations and line colors are identical to Figure 8.

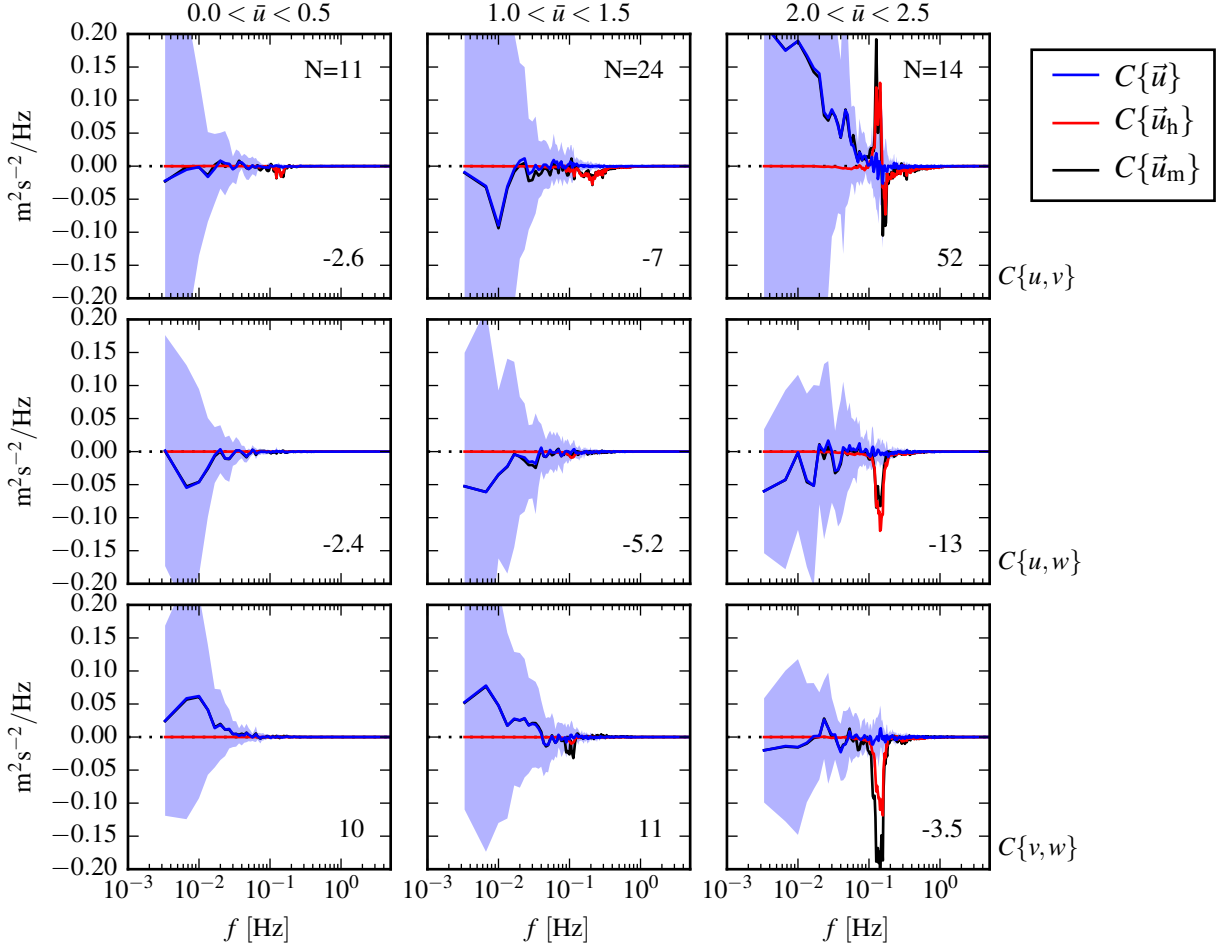


FIG. 11. The real part of the cross-spectral density between velocity components measured by the TTM. The upper row is the u - v cross-spectral density, the middle row is the u - w cross-spectral density, and the bottom row is the v - w cross-spectral density. The columns are for different ranges of the stream-wise mean velocity magnitude (indicated above the top row). The blue line is the cross spectrum between components of motion-corrected velocity, the red line is the cross spectrum between components of head-motion, and the black line is the cross spectrum between components of uncorrected velocity. The light blue shading indicates one standard deviation of the C for the motion-corrected cross-spectral density. N is the number of spectral ensembles in each column. The number in the lower-right corner of each panel is the motion-corrected Reynold's stress (integral of the blue line) in units of $1\text{e-}4 \text{ m}^2\text{s}^{-2}$.

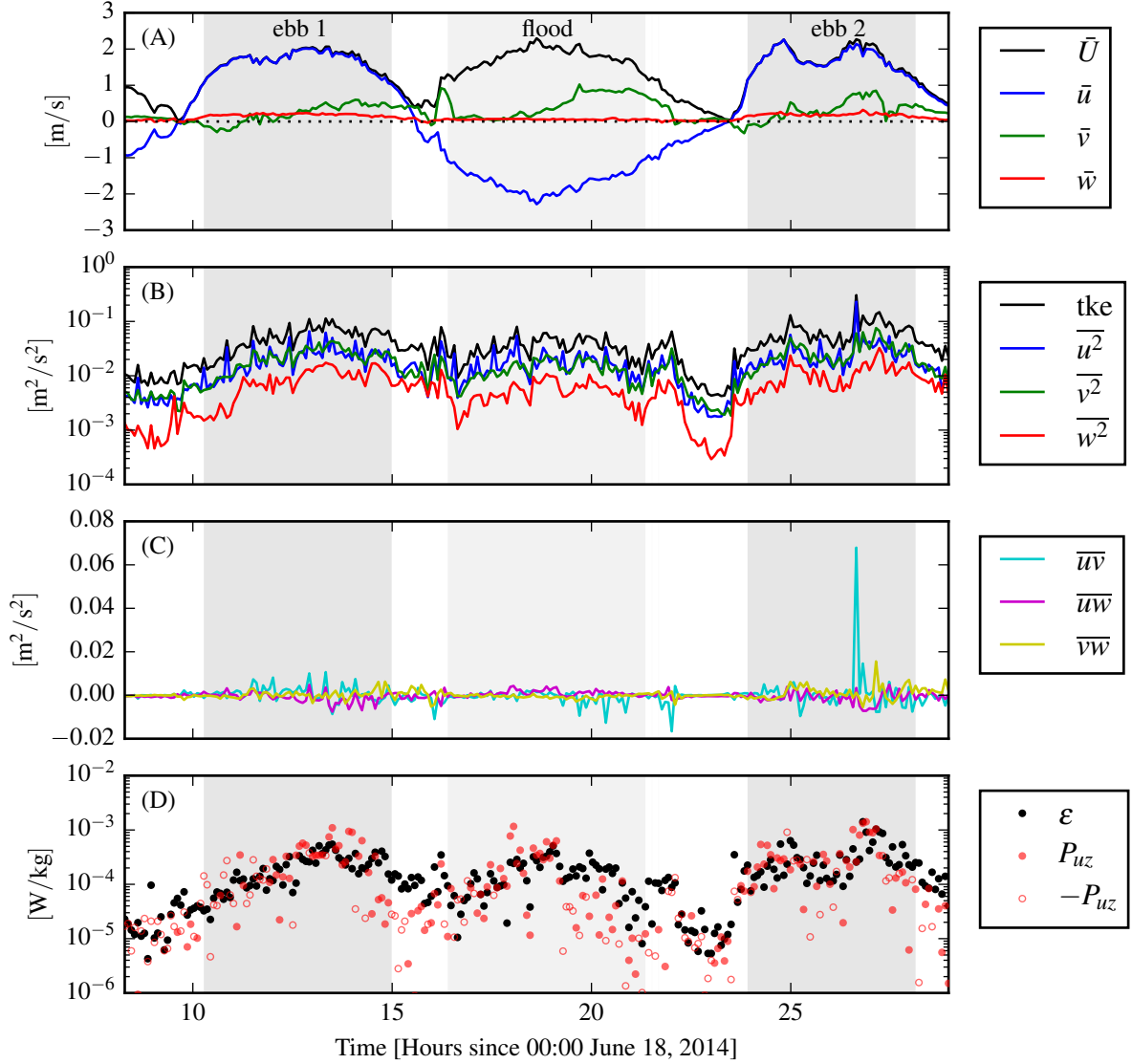


FIG. 12. Time series of mean velocities (A), turbulence energy and its components (B), Reynold's stresses (C), and turbulence dissipation rate (D) measured by the TTM during the June 2014 deployment. Shading indicates periods of ebb ($\bar{u} > 1.0$, grey) and flood ($\bar{u} < -1.0$, lighter grey).

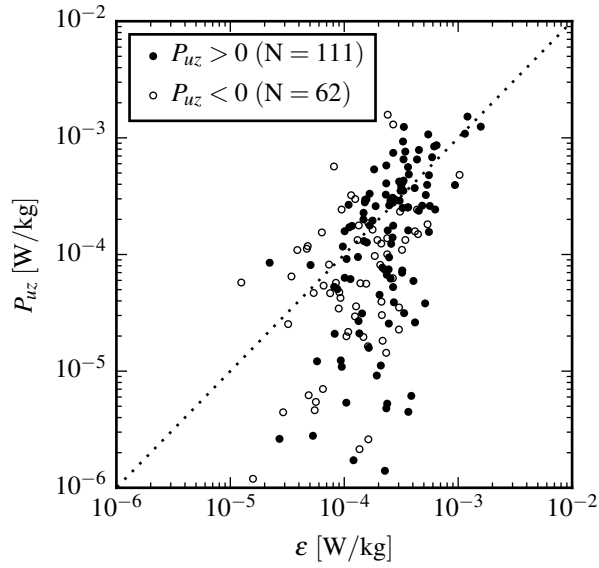


FIG. 13. P_{uz} vs. ε during the June 2014 TTM deployment for values of $|u| > 1$ m/s. Values of negative production are indicated as open circles.

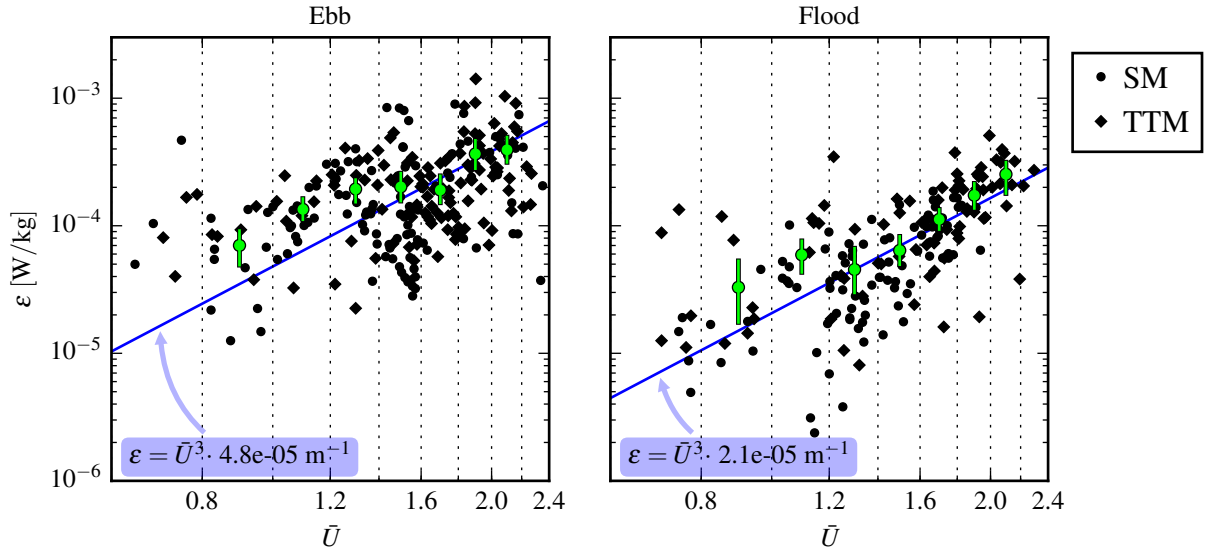


FIG. 14. A log-log plot of ε versus \bar{U} for the June 2014 TTM (diamonds) and May 2015 StableMoor (dots) deployments, during ebb (left) and flood (right). Black points are 5-minute averages. Green dots are mean values within speed bins of 0.2 m s^{-1} width that have at least 10 points (50 minutes of data); their vertical bars are 95% bootstrap confidence intervals. The blue line shows a U^3 slope, wherein the proportionality constant (blue box) is calculated by taking the log-space mean of ε/U^3 .

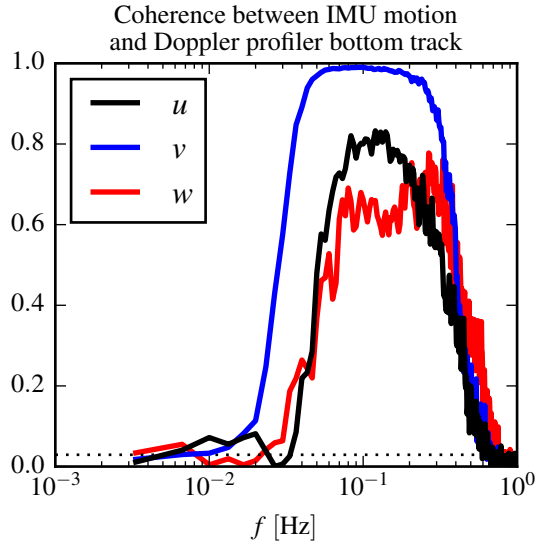


FIG. 15. Coherence between IMU-measured motion of StableMoor buoy and ADP bottom-track velocity for $1.0 < \bar{U} < 1.5$. The horizontal dotted line indicates the 95% confidence level for the 102 spectral windows in this estimate.